



Article submitted to journal

Subject Areas:

Atmospheric Physics and
Meteorology, Climate Science

Keywords:

Extreme rainfall, climate change,
convective organization

Author for correspondence:

P. A. O'Gorman

e-mail: pog@mit.edu

Response of extreme
precipitation to uniform
surface warming in
quasi-global aquaplanet
simulations at high resolution

P. A. O'Gorman¹, Z. Li¹, W. R. Boos² and
J. Yuval¹

¹Department of Earth, Atmospheric and Planetary
Sciences, Massachusetts Institute of Technology,
Cambridge, MA 02139, USA

²Department of Earth and Planetary Science,
University of California, Berkeley, Berkeley, California,
USA

Projections of precipitation extremes in simulations with global climate models are very uncertain in the tropics, in part because of the use of parameterizations of deep convection and model deficiencies in simulating convective organization. Here we analyze precipitation extremes in high-resolution simulations that are run without a convective parameterization on a quasi-global aquaplanet. The frequency distributions of precipitation rates and precipitation cluster sizes in the tropics of a control simulation are similar to the observed distributions. In response to climate warming, 3-hourly precipitation extremes increase at rates of up to $9\% \text{ K}^{-1}$ in the tropics because of a combination of positive thermodynamic and dynamic contributions. The dynamic contribution at different latitudes is connected to the vertical structure of warming using a moist static stability. When the precipitation rates are first averaged to a daily timescale and coarse-grained to a typical global climate-model resolution prior to calculating the precipitation extremes, the response of the precipitation extremes to warming becomes more similar to what was found previously in coarse-resolution aquaplanet studies. However, the simulations studied here do not exhibit the high rates of increase of tropical precipitation extremes found in projections with some global climate models.

1. Introduction

Simulations with global climate models project a general intensification of precipitation extremes in most regions as the climate warms [1,2]. The rate of intensification varies regionally and seasonally because of variations in the dynamic contribution to changes in precipitation extremes which is particularly uncertain in the tropics [3]. The large inter-model differences in the response in the tropics [4] arise partly because of parameterizations of deep convection which are known to strongly affect the intensity distribution of precipitation [5]. Furthermore, the inability of coarse global climate models to represent mesoscale organization of convection calls into question their ability to correctly simulate the response of precipitation extremes to climate change [6], and the role of convective organization in this response is an active area of research [7–9]. A number of studies have analyzed precipitation extremes in regional simulations at high resolution run without a convective parameterization of deep convection [10–12], but because of their regional focus it is difficult to use the results to understand the global response and the role of large-scale dynamics in shaping this response. Global convection permitting simulations are now becoming available [13,14] but they are typically run for too short a time for the analysis of the response of extremes to climate change.

Here we analyze high-resolution simulations without a convective parameterization that are run in an idealized aquaplanet domain that includes both extratropical and tropical dynamical regimes. The use of an idealized domain with a zonally symmetric lower boundary limits the direct applicability of our results to societal impacts, but it simplifies the problem of obtaining physical understanding of changes in precipitation extremes which is very challenging in full-complexity coupled simulations and in observations. Moreover, the zonal symmetry is helpful for obtaining robust statistics of precipitation extremes.

To reduce computational expense, we run our simulations at 12km horizontal grid spacing and use hypohydrostatic rescaling to increase the horizontal length scale of convection while not changing the large-scale dynamics [15,16]. Hypohydrostatic rescaling modifies the inertial term in the dynamical equation for the vertical velocity, and previous studies at grid spacings of 8–40km have found that it improves the representation of tropical cyclones [17,18] and midlatitude precipitation extremes [19], and it has also been used in studies of monsoonal circulations [20]. Even without hypohydrostatic rescaling, simulations at 12km can have a good representation of precipitation when the parameterization of deep convection is turned off [21,22], and the parameterization of deep convection can sometimes be harmful at such a grid spacing [23]. As partial validation, we show here that frequency distributions of precipitation intensity and cluster size in the tropics of our control simulation compare well with observations.

The dynamic contribution to changes in precipitation extremes (i.e., the contribution owing to changes in vertical winds) has been found to be important in projections with global climate models [3] and in idealized aquaplanet simulations [8,24,25]. We highlight here two distinct lines of research that have sought to explain this dynamic contribution at the convective scale and at larger scales, respectively. At the convective scale, high-percentile updrafts in radiative convective equilibrium (RCE) are found to become faster with warming [26,27]. The faster updrafts have been explained using an entraining plume model and an assumption of convective quasi-equilibrium which predicts a decrease in moist static stability (a measure of the difference of the temperature lapse rate from a moist adiabatic lapse rate) as the atmosphere warms [28–30]. Similarly the dynamical response of an entraining plume model to temperature perturbations from a composite sounding in midlatitudes has been found to depend on changes in moist static stability [31]. For vertical velocities associated with precipitation extremes in RCE, the changes in vertical velocities with warming are positive at upper levels but can be negative in the lower troposphere [32]. At larger scales, the quasigeostrophic (QG)- ω equation has been used to understand changes in vertical velocities associated with extratropical precipitation extremes [33–37]. A recent study found that changes in moist static stability play a key role for the magnitude and spatial pattern of changes in vertical velocities within the framework of a

moist QG- ω equation [37]. Thus, both the entraining-plume perspective and the QG- ω equation suggest that changes in moist static stability are important for changes in vertical velocities, and we investigate this influence in our quasi-global simulations with convective organization over a wide range of length scales.

One advantage of analyzing high-resolution quasi-global simulations is that we can consider precipitation on different length and time scales. In particular, many previous studies of precipitation extremes in global climate projections have considered precipitation in grid boxes of order 100km in the horizontal and on daily time scales. Precipitation extremes at different scales may be associated with different types of circulations or parts of weather systems (e.g., the occluded region versus cold front in an extratropical cyclone) and thus may respond differently to climate change. To address this possible scale dependence, we perform an analysis of 3-hourly precipitation extremes on the model grid and an additional analysis in which we spatially coarse-grain the precipitation and average it to a daily time scale prior to calculating the extremes. The daily coarse-grained analysis is more directly comparable to previous studies that analyzed daily precipitation extremes in global climate models.

We first describe the model and simulations (Section 2) and compare the precipitation intensity and cluster-size distributions to observations and a simulation with a global climate model (Section 3). We then analyze the simulated precipitation extremes and their response to climate change (Section 4), and we decompose the response into thermodynamic and dynamic contributions (Section 5). We relate the dynamic contribution to changes in vertical velocities at different vertical levels, which we in turn relate to changes in moist static stability (Section 6). Lastly, we give our conclusions (Section 7).

2. Simulations

The model used is the System for Atmospheric Modeling (SAM) version 6.3 which is an anelastic model in Cartesian coordinates [38]. The bulk microphysics scheme is single moment with relatively simple representations of rain, snow, graupel, cloud water, and cloud ice. Subgrid turbulence is represented with a Smagorinsky-type scheme. The radiation scheme is adapted from the Community Climate Model (CCM3) [39], and the insolation is set at perpetual equinox without a diurnal cycle. The lower boundary is a zonally symmetric ocean with no sea ice and a specified sea-surface temperature (SST) distribution. Simulations are run on an extended equatorial beta plane of length 17280km and width 6912km, equivalent to 78°S to 78°N in latitude and 62° in longitude at the equator. The boundary conditions are periodic in the zonal direction and walls at the poleward boundaries.

The default time step is 24s, and this is adaptively reduced as necessary to prevent violations of the CFL condition. There are 48 vertical levels and the horizontal grid spacing is 12km. To help resolve convection at this horizontal grid spacing, we employ hypohydrostatic rescaling with a scaling factor of 4 which increases the width of convection while not affecting the large-scale dynamics as discussed in the introduction. The reference profile used in the anelastic equations is an observed tropical mean oceanic sounding. Use of the anelastic equations introduces some error that can, for example, affect growth and propagation of midlatitude baroclinic eddies, although it is not found to affect the frequency distribution of precipitation in the tropics or extratropics [40].

We consider both a control simulation and a warm simulation. The control simulation uses the “qobs” SST distribution [41] which decreases from 300.15K at the equator to 273.15 at the poles. This control simulation was used previously in [42] to develop a parameterization of subgrid processes through machine learning. The warm simulation differs from the control simulation by a uniform increase in SST of 4K without any change in CO₂ concentration. Two ensemble members are run for each of the control and warm simulations starting with different random initial conditions. Each ensemble member is run for 700 days with the first 100 days treated as a spinup period and the remaining 600 days used to calculate statistics. All results presented are thus based on a combined 1200 days at statistical equilibrium for each of the control and warm simulations.

Snapshots of 3-hourly column-integrated precipitable water and surface precipitation are shown in Fig. 1. Extratropical cyclones and anticyclones are dominant in midlatitudes, while there are two intertropical convergence zones (ITCZs) at low latitudes. Tropical cyclones are not generated because the peak in SST is at the equator [43], but there are a range of convective systems of different sizes in the tropics whose statistics we compare to observations in the next section. We note that whether there are one or two ITCZs in a simulation with specified and hemispherically symmetric SSTs is expected to be sensitive to a number of factors including the SST distribution and subgrid parameterizations [44]. Previous studies have found a single ITCZ at coarser resolution in the same model and domain as used here [42] and at higher resolution in the same model but with a different domain and some other differences in configuration [45].

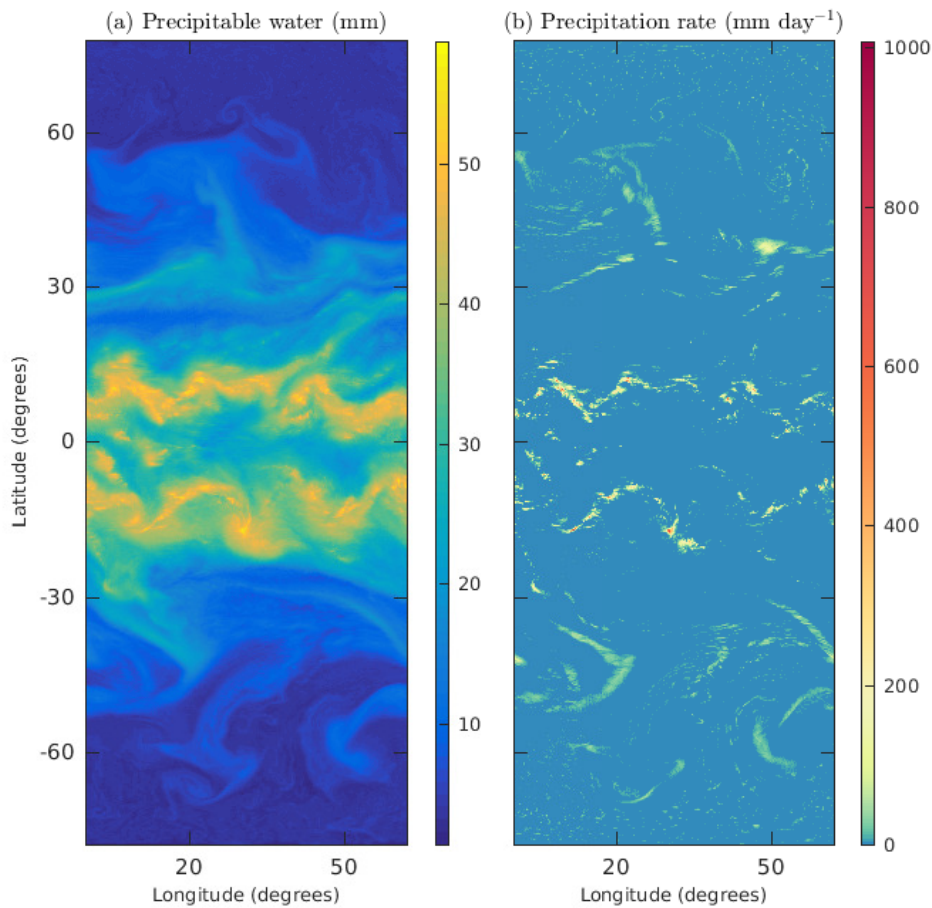


Figure 1. Snapshots of (a) precipitable water (mm) and (b) surface precipitation rate (mm day^{-1}) averaged over a 3-hour period in the control simulation at statistical equilibrium. The model is configured as an equatorial beta plane, and the fields are plotted versus equivalent latitude and longitude. At the largest scales, precipitation is organized by baroclinic eddies in midlatitudes and two ITCZs at low latitudes, but convective organization at a range of length scales is also evident.

3. Comparison of control simulation to observations and a global climate model

We compare precipitation statistics from the control simulation to observations and to a simulation with a coupled global climate model to get a sense of whether the precipitation intensity and multiscale organization are well represented. We first consider the frequency distribution of precipitation rates in the tropics since it varies considerably between global climate models and when different convective parameterizations are used [5,46]. We also consider the frequency distribution of the size of precipitation clusters (distinct groups of spatially connected precipitating grid points) because this allows us to assess convective organization over a wide range of length scales and because it exhibits a known power law in observations that provides a convenient point of comparison [47]. Our idealized model configuration means that the comparison with observations and a coupled climate model is necessarily approximate, but we show that the distributions of precipitation intensity and cluster size from the control simulation are similar to those obtained from observations, suggesting that the simulations are useful for studying precipitation statistics. For observational data, we use the Tropical Rainfall Measurement Mission (TRMM) 3B42 version 7 dataset, which takes inputs from satellite remote sensing and rain gauges [48]. The precipitation rates from this dataset are 3-hourly on a 0.25° longitude by 0.25° latitude grid. For the global climate model simulation, we use ensemble member one from the CESM Large Ensemble (CESM-LE) which gives 6-hourly precipitation rates on an 1.25° longitude by 0.94° latitude grid [49]. In order to make a consistent comparison to CESM-LE, we average in time the 3-hourly precipitation rates from TRMM 3B42 and the control simulation to 6-hourly precipitation rates.

For the control simulation, we consider the region between 15°S and 15°N over 1200 days at statistical equilibrium. For TRMM 3B42 and CESM-LE, we consider a comparable region of the central tropical Pacific between 15°S and 15°N and 160°E and 222°E which is of similar size as the region used in the control simulation and which includes the ITCZ. For TRMM 3B42 and CESM-LE, we use four years of data (01/01/2002 to 12/31/2005) to give a comparable amount of time as in the control simulation while being a whole number of years.

We first consider the frequency distribution of the 6-hourly precipitation rate (Fig. 2a). The distribution is estimated using 30 bins that are approximately equally spaced in the logarithm of precipitation rate for each dataset. The lowest bin starts at 1 mm day^{-1} , but the distribution is normalized such that it integrates to one when all precipitation rates are included (including those smaller than 1 mm day^{-1}). Thus it is the probability distribution function of all precipitation rates including zero precipitation rates. Since the distribution of precipitation rates is affected by grid spacing [50], the precipitation rates from TRMM 3B42 and the control simulation are first conservatively interpolated using spatial averaging to the CESM-LE horizontal grid. There is good agreement between the distributions from the control simulation and TRMM 3B42, especially when compared to the large biases in the CESM-LE distribution in this region. The control simulation does underestimate the frequency of the most extreme precipitation rates as compared to observations, and this may be related to a lack of tropical cyclones in the simulation.

To address the multiscale organization of convection, we next consider the frequency distribution of precipitation cluster size where size refers to the area of the cluster (Fig. 2b). Precipitation rates are considered on the native spatial grids for each dataset and at the 6-hourly time scale. Precipitation clusters are defined here as distinct groups of spatially connected precipitating grid points, where grid points are taken to be connected if they are nearest neighbors (each grid point has four nearest neighbors). Precipitating grid points are defined as gridpoints with precipitation exceeding 0.7 mm h^{-1} , which is one of the thresholds used in a previous study of cluster statistics [47]. Using a lower precipitation threshold gives a similar level of agreement between the control simulation and TRMM 3B42, but CESM-LE becomes less similar to TRMM 3B42 because of too much drizzle in CESM-LE. We normalize the cluster size distribution function such that it integrates to the time mean of the number of clusters per unit area of the domain. The

distribution is estimated using 25 bins that are approximately equally spaced on a log scale of cluster size for each dataset following the approach of [47]. Power-law exponents are estimated using linear regression in log-log space over the first 17 bins.

The cluster size distributions exhibit a power law range and an exponential roll off at the largest cluster sizes (Fig. 2b). The exponent of the power law range for TRMM 3B42 is estimated to be -1.69 which is consistent with a previous estimate of -1.7 [47]. The cluster size distribution from the control simulation compares favorably to TRMM 3B42 with a similar power-law exponent of -1.73, although the exponential roll off for the control simulation occurs at a smaller cluster size than in TRMM 3B42, likely related to the large-scale structure of the ITCZs being different in our idealized simulation. CESM-LE has a much narrower range of cluster sizes given its coarser resolution, and it exhibits a substantially shallower power law with an exponent of -1.21.

Based on Fig. 2, we conclude that the control simulation exhibits spatial organization of precipitation over a wide range of length scales, and that the model is doing a reasonable job of simulating the distributions of tropical precipitation intensity and cluster size, at least to the extent that can be expected given the idealized domain and lower boundary.

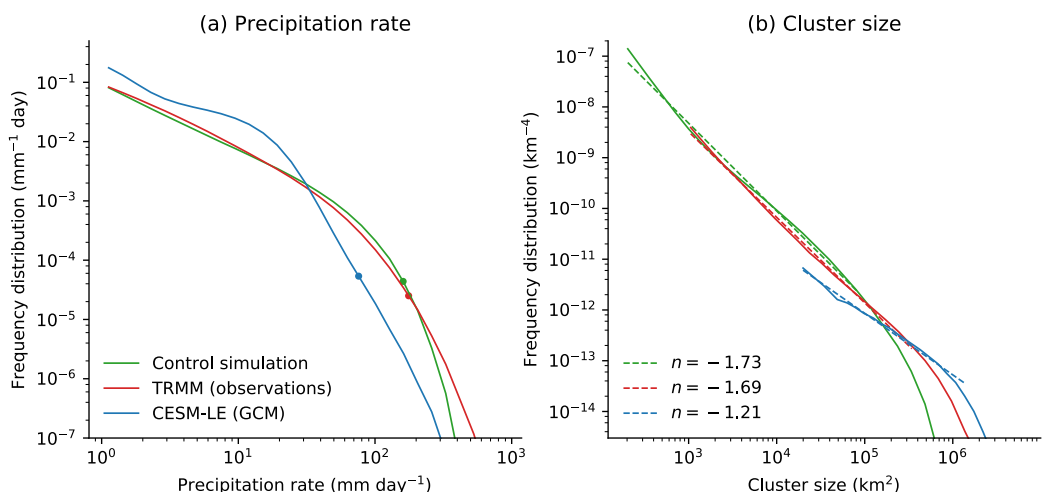


Figure 2. Distributions of tropical (a) precipitation rate and (b) precipitation cluster size for the control simulation (green), TRMM 3B42 observations (red), and the CESM-LE global climate model simulation (blue). Results in this figure are based on 6-hourly precipitation rates. In (a), precipitation rates from the control simulation and TRMM 3B42 have been conservatively interpolated onto the CESM-LE horizontal grid prior to calculating the distribution, and the 99.9th percentiles are shown by filled circles. In (b), power laws are shown for comparison (dashed) with the exponents given in the legend. The data are from all longitudes and $15^\circ\text{S}-15^\circ\text{N}$ for the control simulation, and from the central tropical Pacific ($15^\circ\text{S}-15^\circ\text{N}$, $160^\circ\text{E}-222^\circ\text{E}$) for TRMM 3B42 and CESM-LE.

4. Precipitation extremes and their response to climate warming

We next consider precipitation extremes and their response to climate change. For a given climate, we define extreme precipitation events at a given latitude as exceedances of a high percentile of precipitation (the 99.9th percentile for 3-hourly precipitation) at that latitude. The intensity of precipitation extremes is then calculated as the average of the precipitation rate over all the extreme events at that latitude. We use this definition of the intensity of precipitation extremes rather than just using the percentiles of precipitation directly because it allows us to consistently define other quantities associated with precipitation extremes. In particular, temperatures, vertical velocities and static stabilities associated with the precipitation extremes at a given latitude are

calculated by averaging these quantities over all extreme precipitation events at that latitude. The temperatures and vertical velocities associated with the precipitation extremes (denoted T_e and w_e) are then used to calculate a scaling approximation for the precipitation extremes as discussed later in this section. To reduce noise, a moving average filter of width 12° in latitude is applied to the precipitation extremes, the scaling approximation of precipitation extremes, and the vertical velocities and static stabilities associated with precipitation extremes. Note that the moving average filter is applied prior to calculating fractional changes in response to climate change.

We primarily consider extremes of 3-hourly precipitation on the model grid using exceedances of the 99.9th percentile of precipitation. But we are also interested in the behavior of precipitation extremes at coarser space and time scales that have been widely considered in previous global modeling studies and which may respond differently to climate change from the 3-hourly precipitation extremes. To study precipitation extremes at coarser scales, we spatially coarse-grain the precipitation rates (and other quantities such as temperature and vertical velocities) using area averaging over 8×8 blocks to give a coarser grid spacing of 96km, and we average in time to the daily time scale. Precipitation extremes are then calculated as before but now for daily coarse-grained precipitation. We consider the 99.2th percentile for the daily coarse-grained precipitation extremes for two reasons. First, the 99.2th percentile of daily precipitation corresponds to the same return period as the 99.9th percentile of 3-hourly precipitation. Second, the coarsening in time and space reduces the sample size, and thus using a somewhat lower percentile is helpful for reducing noise.

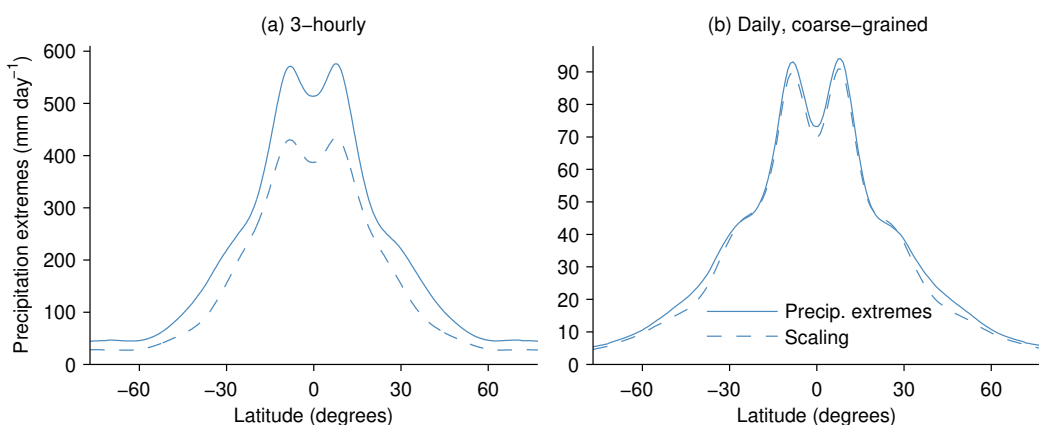


Figure 3. Precipitation extremes (solid) and the precipitation extremes scaling estimate (dashed) versus latitude in the control simulation. Results are shown for (a) 3-hourly precipitation on the model grid and (b) daily precipitation that is spatially coarse-grained to a horizontal grid spacing of 96km prior to calculating the extremes. Precipitation extremes are defined by the average of precipitation rates over all exceedances of the 99.9th percentile for 3-hourly precipitation and the 99.2nd percentile for daily precipitation to give the same return period in each case. In this and subsequent figures, differences between the hemispheres are primarily indicative of sampling errors.

The intensity of precipitation extremes decreases from the tropics to high latitudes, and a signature of the double ITCZ is also evident in the tropics (Fig. 3). The peak values are 576 mm day^{-1} for 3-hourly precipitation extremes and 94 mm day^{-1} for daily coarse-grained precipitation extremes.

We express the sensitivity of precipitation extremes to climate change as the percent change relative to the control climate and normalized by the 4K increase in SST (Fig. 4). For 3-hourly precipitation extremes, the response varies from $4.9\% \text{ K}^{-1}$ to $10.0\% \text{ K}^{-1}$ across all latitudes with a tropical average response of $7.3\% \text{ K}^{-1}$ and a similar extratropical average of $7.5\% \text{ K}^{-1}$ (Fig. 4a).

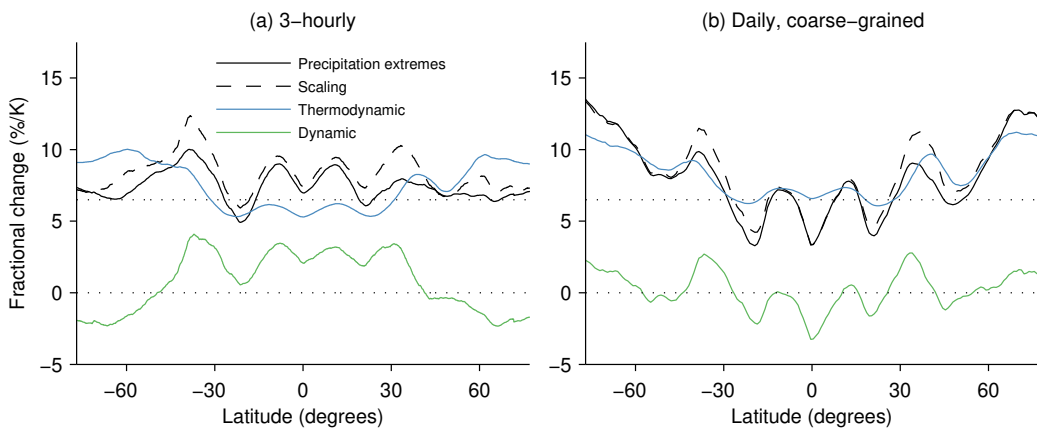


Figure 4. Response of precipitation extremes to climate warming (black solid), the response as estimated by the precipitation extremes scaling (black dashed), and the decomposition of the response into thermodynamic (blue) and dynamic (green) contributions. Results are shown for (a) 3-hourly precipitation on the model grid and (b) daily precipitation that is spatially coarse-grained to a horizontal grid spacing of 96 km prior to calculating the extremes. The horizontal dotted lines show reference values of 0 and $6.5\% \text{ K}^{-1}$. All results shown are normalized by the change in SST of 4 K.

Tropical and extratropical averages are taken equatorward and poleward of 30° , respectively. Within the tropics, there is a stronger response in the ITCZ regions with a maximum rate of increase across tropical latitudes of $9.0\% \text{ K}^{-1}$. Higher rates of change are typically found for higher percentiles. For example, the tropical average rate of increase for 3-hourly precipitation extremes increases from $7.3\% \text{ K}^{-1}$ for the 99.9th percentile to $8.3\% \text{ K}^{-1}$ for the 99.99th percentile.

The daily coarse-grained precipitation extremes exhibit a somewhat different response, with a weaker response in the tropics ($5.6\% \text{ K}^{-1}$) and a stronger response in the extratropics ($9.6\% \text{ K}^{-1}$) that peaks at high latitudes with values close to $14\% \text{ K}^{-1}$ (Fig. 4b). Both the averaging to a daily time scale and the spatial coarse graining contribute to the difference in responses between 3-hourly precipitation extremes and daily coarse-grained precipitation extremes. Considering the 99.9th percentile instead of the 99.2nd percentile for the daily coarse-grained precipitation extremes reduces the difference in response compared to 3-hourly precipitation extremes in the tropics but the latitudinal distributions of the responses still remain different.

Previous studies of daily precipitation extremes on aquaplanets with coarse-resolution global climate models have found a stronger sensitivity of precipitation extremes to climate change at high latitudes as compared to the tropics [24,25], similar to what we find here for daily coarse-grained precipitation extremes. It is notable that this polar amplified response of precipitation extremes does not occur for the 3-hourly precipitation extremes on our higher-resolution grid, and we investigate this further in the next section.

5. Thermodynamic and dynamic contributions

We next use a scaling approximation for precipitation extremes to determine the thermodynamic and dynamic contributions to changes in precipitation extremes at each latitude. Our aim in making this decomposition is to better understand the variation in sensitivity across latitudes and the differing sensitivities when 3-hourly and daily coarse-grained precipitation extremes are considered. The scaling approximation was derived assuming saturated moist adiabatic ascent [1] or using a dry static energy budget in the tropics without assuming saturated ascent [32], and it has been used in a number of studies to relate the precipitation rate to the vertical profiles of temperature and vertical velocity in extreme precipitation events [3,36,51–54]. We refer to it as a scaling approximation because it estimates the vertically integrated net condensation rate and

thus only predicts the precipitation rate up to a factor that can be thought of as a precipitation efficiency. Nonetheless, this factor is close to one for precipitation averaged over sufficiently large space and time scales [3,55].

For the anelastic SAM model which uses a reference density profile $\rho_0(z)$ as a function of height z , the scaling approximation may be written as

$$P_e \sim - \int_0^{z_t} \rho_0(z) w_e(z) S(T_e, z) dz \quad (5.1)$$

where P_e is the surface precipitation rate in the extreme event, $w_e(z)$ is the vertical velocity associated with precipitation extremes, $S(T_e, z)$ is a thermodynamic factor that is evaluated at the temperature T_e associated with precipitation extremes, and z_t is the tropopause height diagnosed from the lapse rate of T_e .

The thermodynamic factor S is the derivative of the saturation mixing ratio $q_{\text{sat}}(T, p)$ with respect to z assuming a moist-adiabatic lapse rate of temperature, and it may be written as

$$S \equiv \left(\frac{dq_{\text{sat}}}{dz} \right)_{\text{ma}} = \frac{\partial q_{\text{sat}}}{\partial p} \frac{dp}{dz} + \frac{\partial q_{\text{sat}}}{\partial T} \left(\frac{\partial T}{\partial z} \right)_{\text{ma}}, \quad (5.2)$$

where $p(z)$ is the horizontal-average pressure profile and subscript ma denotes moist adiabatic. In evaluating $S(T_e, z)$, the moist adiabatic lapse rate $(\partial T / \partial z)_{\text{ma}}$ is calculated using T_e at each vertical level. We use T_e rather than the temperature of a parcel lifted moist adiabatically from near the surface in order to avoid making assumptions about which parcel to lift or the extent to which the stratification is moist adiabatic.

For the case of 3-hourly precipitation, we use the instantaneous values of w_e and T_e at the start of the 3-hour period because only instantaneous velocities and temperatures were stored. Using an average of the instantaneous w_e and T_e values at the start and end of the 3-hour period gives lower values of the scaling approximation in the control climate, presumably because condensation is occurring to a greater extent at the start of the period. For daily precipitation extremes, we average 8 values of w_e and T_e that are spaced every 3 hours and start at the beginning of the 24 hour period.

In the control climate, the scaling approximation underestimates the 3-hourly precipitation extremes by about 25% but the shape of the latitudinal distribution is well captured (Fig.3a). Rather than implying a precipitation efficiency larger than one, the underestimate is likely because instantaneous rather than 3-hourly w_e and T_e were used which means that the peak in condensation is likely not captured. The agreement is excellent for the daily coarse-grained precipitation extremes at all latitudes (Fig.3b). Importantly, the scaling approximation captures the response to climate change with a slight overestimate of the response for the 3-hourly precipitation extremes (Fig.4a) and generally good agreement for the daily coarse-grained precipitation extremes (Fig.4b), suggesting that changes in precipitation efficiency are relatively unimportant (although this may be sensitive to the precipitation microphysics used at lower temperatures [51]).

We next use the scaling approximation to decompose the total response of precipitation extremes into a contribution from changes in T_e and p (the thermodynamic contribution) and changes in w_e (the dynamic contribution). To evaluate the thermodynamic contribution, we use the average of w_e between the two climates as input to the scaling approximation in each climate and then calculate the change in the scaling approximation in response to climate warming. To evaluate the dynamic contribution, we use the averages of T_e and p between the two climates as inputs to the scaling approximation in each climate and then calculate the change in the scaling approximation in response to climate warming. The thermodynamic and dynamic contributions are expressed in $\% \text{ K}^{-1}$ by normalizing by the full scaling in the control climate and by the change in SST (4K). With this approach to calculating the thermodynamic and dynamic contributions, their sum differs from the total scaling response by less than $0.1\% \text{ K}^{-1}$ at all latitudes. The remainder term involving a product of dynamic and thermodynamic changes is negligible

because we use the average between climates for the variables that are held constant in each contribution as opposed to using just the control-climate values.

For both the 3-hourly precipitation extremes and the daily coarse-grained precipitation extremes, the thermodynamic contribution is substantially stronger at high latitudes than in the tropics (Fig. 4a,b). This is due to the thermodynamic factor $S(T_e, z)$ having larger fractional increases with warming at lower temperatures (see Fig. S2 of [1]). Note that the strong thermodynamic contribution at higher latitudes is not due to polar amplified warming since polar amplification is limited in our simulations by the uniform increase in SST. Even when a uniform increase in SST is not imposed, polar amplification of warming occurs primarily for the mean temperature rather than T_e [24]. The meridional gradient in the thermodynamic contribution is less prominent in coupled-climate model projections for annual extremes because extremes at high latitudes can occur in the warm season [56], but a particularly large thermodynamic contribution can be seen at northern high latitudes in winter (see Fig. S7c of [3]). In the tropics, the thermodynamic contribution is close to Clausius-Clapeyron scaling with near-surface temperature. This scaling with near-surface temperature has been noted before but it is somewhat surprising since much of the convergence of water vapor occurs higher in the atmosphere, and the cause for this scaling has recently been found to be the universal shape of vertical velocity profiles conditioned on extreme precipitation events when expressed in a moisture vertical coordinate [54].

For 3-hourly precipitation extremes, the dynamic contribution is positive at low latitudes and negative at high latitudes. The positive dynamic contribution at low latitudes differs from a negative dynamic contribution to changes in precipitation extremes in small-domain RCE [32,54] and this discrepancy may relate to the presence of organized convection in our simulations (see also [7]). For daily coarse-grained precipitation extremes, the dynamic contribution is mostly negative in the tropics and positive at high latitudes, but there is not as clear a poleward shift of the vertical velocities as was found in previous studies of daily precipitation extremes in aquaplanet climate models [24,25].

Thus, the responses for both 3-hourly and daily coarse-grained precipitation extremes can be understood through a combination of the thermodynamic and dynamic contributions. Stronger thermodynamic contributions at higher latitudes play an important role in both cases, and differences in the latitudinal distributions of the response between the 3-hourly and daily coarse-grained precipitation extremes are primarily due to the dynamic contribution.

One limitation of our simulations is that the reference density profile used in the anelastic approximation in SAM was the same for both the control and warm climates whereas it should decrease with warming. By changing the density profile in the precipitation extremes scaling (Eq. 5.1), we estimate that the decrease in density with warming would decrease the response of precipitation extremes to climate warming by roughly $0.5\% \text{ K}^{-1}$ assuming there is no compensation in the changes in w_e .

6. Relation of dynamic contribution to changes in vertical velocities and moist static stability

To better understand the dynamic contribution, we next consider the changes in vertical velocities at different vertical levels and how these changes relate to changes in moist static stability.

We first consider the dynamic contribution to changes in precipitation extremes at different vertical levels which is calculated as $-\rho_0 \delta w_e S$ where δw_e is the change in w_e between the two climates and the thermodynamic factor S is evaluated using the averages of T_e and p between the two climates (cf. Equation 5.1). For 3-hourly precipitation (Fig. 5a), the dynamic contribution in the tropics is positive in the middle troposphere and more weakly negative in the lower troposphere, such that the total contribution is positive when integrated vertically. At high latitudes, the dynamic contribution is negative in the lower troposphere leading to a negative total contribution. Changes in w_e (Fig. 5c) show a similar pattern except they extend

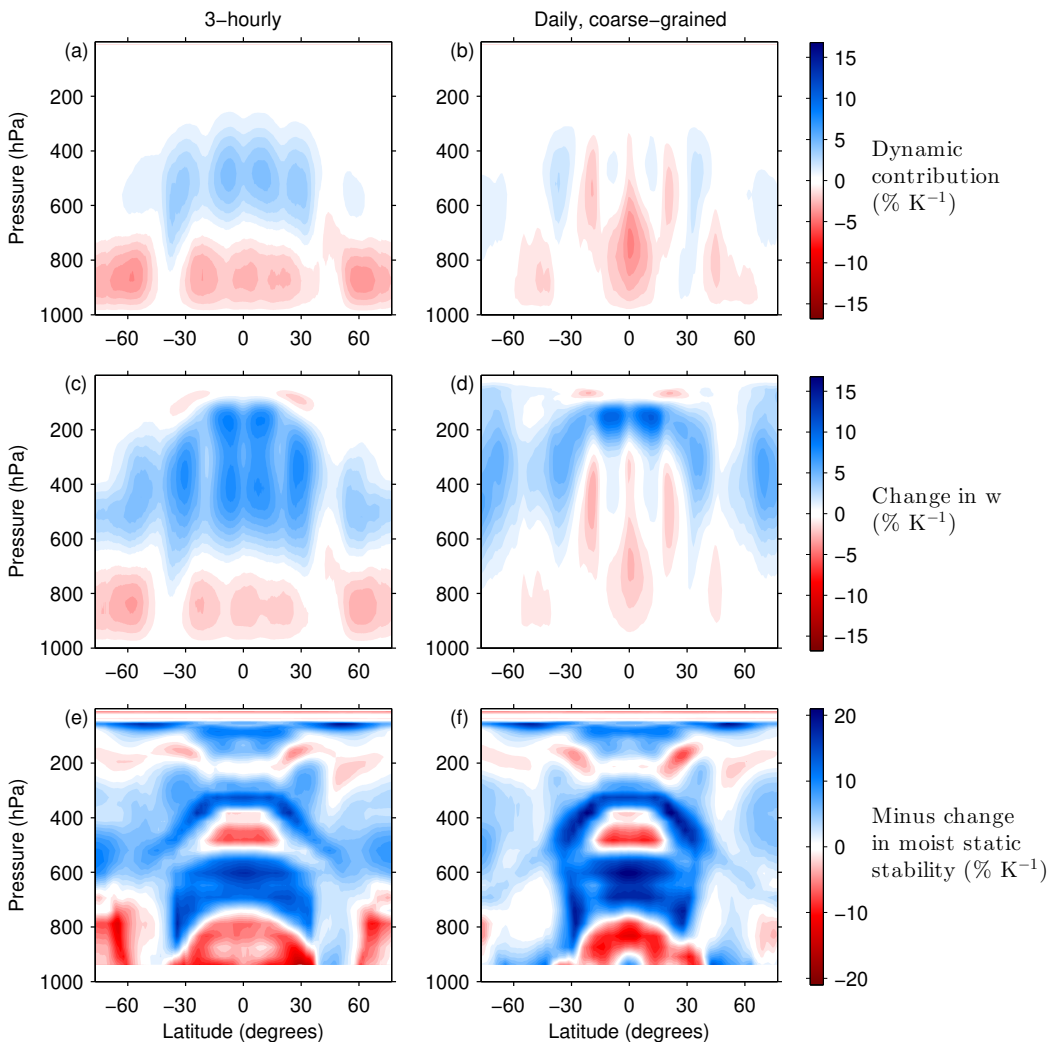


Figure 5. Changes ($\% \text{ K}^{-1}$) in dynamics and moist static stability associated with precipitation extremes in response to climate change: (a,b) the dynamic contribution to changes in precipitation extremes, (c,d) changes in vertical velocities associated with precipitation extremes, and (e,f) minus the changes in moist static stability associated with precipitation extremes. Results are shown for (a,c,e) 3-hourly precipitation on the model grid and (b,d,f) daily precipitation that is spatially coarse-grained to a horizontal grid spacing of 96km prior to calculating the extremes. The dynamic contribution (a,b) and vertical velocities (c,d) are normalized by the maximum over all vertical levels of the control-climate values at that latitude. Changes in moist static stability (e,f) are normalized by the greater of 0.5 K km^{-1} and the control-climate value at that latitude and vertical level (the fixed minimum is used to avoid dividing by small or zero values in the tropics). All results are also normalized by the change in SST of 4K. Changes are calculated on model z levels but plotted versus pressure in the control climate to better emphasize the lower and middle troposphere. Changes in moist static stability are not shown below 950hPa.

higher into the upper troposphere where the dynamic contribution to changes in precipitation extremes is limited by small saturation vapor pressures. The changes in vertical velocities in the tropics are consistent with previous studies of radiative convective equilibrium (RCE) which generally show increases in updraft speed with warming [26,27] but negative changes in the lower

troposphere for vertical velocities associated with precipitation extremes [32]. For daily coarse-grained precipitation extremes (Fig. 5b), the dynamic contribution in the tropics is negative in the lower troposphere and somewhat negative in the middle troposphere, leading to an overall negative contribution. Updraft speeds do increase in the upper troposphere as for the 3-hourly precipitation extremes (Fig. 5d).

It has previously been argued based on an entraining plume model that faster updrafts with warming in the tropics are related to a decrease in moist static stability [27–30]. This result and another study with an entraining plume model in the extratropics [31] motivate us to consider a simple moist static stability defined as $\partial T_e/\partial z - (\partial T/\partial z)_{ma}$, where $\partial T_e/\partial z$ is the negative of the temperature lapse rate associated with precipitation extremes, and $(\partial T/\partial z)_{ma}$ is the negative of the moist adiabatic lapse rate evaluated using T_e at each vertical level. Based on a plume-model argument, a more negative moist static stability at a given level is expected to lead to faster updrafts at levels higher in the atmosphere.

In terms of the dry static energy, s , the moist static stability may be alternatively written as $(\partial s_e/\partial z - (\partial s/\partial z)_{ma})/c_p$ where c_p is the specific heat capacity of air at constant pressure and s_e is the dry static stability associated with precipitation extremes. Written in this way, the moist static stability is very similar to the moist static stability that emerged as a key parameter when a moist QG- ω equation was used to understand contributions to changes in extratropical precipitation extremes [37]. Thus, both at the convective scale in the tropics and at larger scales governed by balanced dynamics in the extratropics, changes in vertical velocities may be expected to be related to changes in moist static stabilities (as well as other factors such as large-scale advective forcing in the case of the QG- ω equation). The moist QG- ω equation is not applicable at low latitudes because of small values of the Coriolis parameter and moist static stability.

The moist static stability associated with precipitation extremes in the control climate is negative in the tropical lower and middle troposphere and generally positive elsewhere (not shown). In Fig. 5(e,f), we plot the negative of the change in moist static stability associated with precipitation extremes so that blue colors in Fig. 5 correspond to both increases in upward motion and decreases in moist static stability. Changes in both $\partial T_e/\partial z$ and $(\partial T/\partial z)_{ma}$ contribute to the changes in moist static stability. Changes in the dry static stability as measured by changes in $\partial T_e/\partial z$ are generally positive, but changes in the moist static stability can be positive or negative depending on the latitude and vertical level.

For 3-hourly precipitation extremes, the moist static stability in the tropics decreases between 300hPa and 400hPa and between 600hPa and 800hPa, and increases in the lower troposphere (Fig. 5e). Moist static stability also increases in a region near 500hPa that may be related to melting and freezing of condensates. Interpreted through a plume model, the updraft speed at a given vertical level depends on the moist static stability at lower levels. Thus we would expect the changes in moist static stability to lead to decreases in updraft speed in the lower troposphere and increases in the middle and upper troposphere (assuming that the increased moist static stability near the melting level is outweighed by the larger region of decreased moist static stability below it). These expectations for the tropics are consistent with the changes in updraft speeds in Fig. 5c.

In the extratropics, we can either interpret the changes in w_e through the moist QG- ω equation where the atmosphere is convectively stable or through the plume model where it is unstable. With either interpretation, the decreases in moist static stability in the middle troposphere and increases in the lower troposphere are consistent with increases in vertical velocities in the middle troposphere and decreases in the lower troposphere.

The percentage changes of updraft speeds and moist static stability also roughly agree in magnitude. Closer agreement is not expected because of entrainment (which reduces the magnitude of increases in updraft speeds [27]) and because the plume argument links the updraft speed at a given vertical level to the moist static stability integrated over lower levels. Furthermore, the normalization of changes in moist static stability in Fig. 5e,f involves a fixed minimum value to avoid dividing by zero in the tropical middle and lower troposphere. Absolute changes in moist static stability are shown for reference in Supplementary Figure 1.

For daily coarse-grained precipitation extremes (Fig. 5f), there is not a clear correspondence between the changes in vertical velocities and moist static stability in the tropics which is not surprising given that the plume model argument is not applicable at such coarse length scales. However, the changes in moist static stability and vertical velocities do show some consistency in the extratropics (where the moist QG- ω equation is applicable), with increases in vertical velocities and decreases in moist static stability in the upper troposphere. In particular, there is little to no increase in moist static stability and no corresponding decrease in upward motion in the lower troposphere at high latitudes in contrast to the changes for 3-hourly extremes. An upward shift of the circulation and tropopause with climate warming is likely also contributing to the response of vertical velocities in the middle and upper troposphere [54,57].

Overall these results show the importance of different changes in vertical velocities at different levels of the atmosphere for the dynamic contribution to changes in precipitation extremes, and they also show the potential of a moist static stability for better understanding the changes in vertical velocities.

7. Conclusions

We have studied the response of precipitation extremes to climate change in high-resolution simulations run without the use of a convective parameterization in an idealized quasi-global domain over ocean. Comparison with observations suggests that the simulations have a good representation of the distribution of precipitation rates in the tropics. The simulations also exhibit precipitation clusters over a wide range of scales with a power-law dependence similar to observations. The use of an idealized configuration with a zonally symmetric ocean as lower boundary facilitates the estimation of precipitation extremes and the development of physical understanding of the response of the precipitation extremes to climate change.

For 3-hourly precipitation extremes on the model grid, the response of the intensity of precipitation extremes is in the range 4.9–10.0% K⁻¹ across latitudes with similar average sensitivities in the tropics and extratropics. To compare with previous work with global models, we also analyzed precipitation rates that were first averaged to the daily timescale and spatially coarse-grained to a typical grid spacing in a global climate model prior to calculating extremes. The sensitivity of the daily coarse-grained precipitation extremes to warming was found to be stronger at higher latitudes and weaker in the tropics as compared to the 3-hourly precipitation extremes and more similar to what has been found for daily precipitation in coarser-resolution climate-model simulations of aquaplanets. Thus the dependence on latitude of the response of precipitation extremes depends on the time and length scales over which precipitation is measured.

We used a physical scaling approximation for precipitation extremes to diagnose the thermodynamic and dynamic contributions to changes in precipitation extremes. The thermodynamic contribution is stronger at higher latitudes due to the low temperatures at these latitudes. For 3-hourly precipitation extremes, the dynamic contribution is positive in the tropics (due to stronger updrafts in the middle troposphere that outweigh weaker updrafts in the lower troposphere) and negative at high latitudes (due to weaker updrafts in the lower troposphere). By contrast, for daily coarse-grained precipitation extremes, negative changes in vertical velocities in the tropical lower and middle troposphere give rise to a negative dynamic contribution in the tropics. Changes in vertical velocities seem to be linked to changes in moist static stability in both the tropics and extratropics for 3-hourly precipitation extremes and in the extratropics for daily coarse-grained precipitation extremes.

Future work should investigate the different contributions in addition to changes in moist static stability in the extratropics (possibly using the QG- ω equation applied to the coarse-grained fields) and should also investigate the extent to which the zero-buoyancy plume model [27–30,54] can explain the changes in moist static stability and vertical velocities in the tropics. Changes in moist static stability associated with precipitation extremes have many similarities but also some differences with changes in a moist static stability calculated from zonal- and time-mean

temperatures (compare Supplementary Figs. 1 and 2), and these similarities and differences are worthy of further study.

A previous study of daily precipitation extremes at the 99.9th percentile in the tropics estimated a sensitivity to climate change of 6–14% K^{−1} by constraining projections from coupled climate models using observations of interannual variability [4]. If the 99.9th percentile is considered for daily coarse-grained precipitation extremes in our simulations (rather than the 99.2nd percentile), the sensitivity averaged over the tropics increases from 5.6% K^{−1} to 7.0% K^{−1} which is within the range estimated in [4]. The same observational constraint applied to projections for the extratropics gives a sensitivity of 6–7 % K^{−1} [33] which is lower than what we find here for the 99.9th percentile of daily coarse-grained precipitation extremes (9.6% K^{−1}). This discrepancy in the extratropics likely relates to the strong thermodynamic contribution at the cold high latitudes in our idealized simulations without a seasonal cycle, whereas annual precipitation extremes at high latitudes in coupled climate model simulations can occur in the warm season [56] leading to a smaller thermodynamic contribution. The 3-hourly precipitation extremes in our simulations do show a dynamic contribution that is substantially more positive in the tropics than at high latitudes, which could lead to a higher sensitivity of precipitation extremes in the tropics than at high latitudes if the thermodynamic contribution was more uniform with latitude in simulations with a seasonal cycle. The 3-hourly precipitation extremes also show a relatively high sensitivity in the ITCZ regions (up to 9 % K^{−1}), but none of the tropical-average sensitivities in our study reach the high values found in a few global climate models of up to 23 % K^{−1} [4]. Studies with a superparameterized climate model [53] and a high-resolution simulation configured in a tropical channel [54] also do not find such high sensitivities, and they may well be an artifact of the convective parameterizations used in some global climate models.

We have used a 12km horizontal grid spacing with hypohydrostatic rescaling to reduce computation expense. Previous studies have found hypohydrostatic rescaling to be useful in the simulation of tropical cyclones, precipitation extremes, and monsoonal circulations. Our simulations show a favorable comparison with observed tropical precipitation, but it is important to further validate the use of hypohydrostatic rescaling by additional comparisons with higher-resolution simulations in future work. Global high-resolution simulations run without deep convective parameterizations clearly have great potential for studies of climate impacts [14] and for developing new parameterizations using machine learning [42,58–60]. The results presented here also illustrate their value for idealized studies of precipitation over a wide range of scales in both tropical and extratropical regimes, all in a single model. Future work could further explore the response of precipitation extremes to climate change in this type of idealized high-resolution configuration with different SST distributions or with the inclusion of continents and topography.

Data Accessibility. CESM-LE output is available at:

https://www.earthsystemgrid.org/dataset/ucar.cgd.cesm4.CESM_CAM5_BGC_LE.html

TRMM 3B42 data are available at: <https://disc.gsfc.nasa.gov/datasets?keywords=TMPA&page=1>

Output from the SAM simulations is available at <https://pog.mit.edu/publications.html> and <https://boos.berkeley.edu>.

Authors' Contributions. POG and WRB conceived of and designed the study. WRB, JY and ZL ran the simulations. POG and ZL performed the analysis of model output and observations. POG drafted the manuscript. All authors edited the manuscript.

Competing Interests. The authors declare that they have no competing interests.

Funding. PAOG and ZL acknowledge support from NSF AGS-1552195. JY acknowledges support from the EAPS Houghton-Lorenz postdoctoral fellowship. WRB acknowledges support from the U.S. Department of Energy, Office of Science, Biological and Environmental Research under award DE-SC0019367. We acknowledge high-performance computing support from Cheyenne (doi:10.5065/D6RX99HX) provided by NCAR's Computational and Information Systems Laboratory and sponsored by the National Science Foundation.

Acknowledgements. We acknowledge Marat Khairoutdinov for making SAM available to the community. We also acknowledge the CESM Large Ensemble Community Project. TMPA data were provided by the

NASA/Goddard Space Flight Center's Mesoscale Atmospheric Processes Laboratory and PPS, which develop and compute the TMPA as a contribution to TRMM.

References

- O'Gorman PA, Schneider T. 2009 The physical basis for increases in precipitation extremes in simulations of 21st-century climate change. *Proc. Natl. Acad. Sci.* **106**, 14773–14777.
- Kharin VV, Zwiers FW, Zhang X, Wehner M. 2013 Changes in temperature and precipitation extremes in the CMIP5 ensemble. *Clim. Chang.* **119**, 345–357.
- Pfahl S, O'Gorman PA, Fischer EM. 2017 Understanding the regional pattern of projected future changes in extreme precipitation. *Nat. Clim. Change* **7**, 423–427.
- O'Gorman PA. 2012 Sensitivity of tropical precipitation extremes to climate change. *Nature Geo.* **5**, 697–700.
- Wilcox EM, Donner LJ. 2007 The frequency of extreme rain events in satellite rain-rate estimates and an atmospheric general circulation model. *J. Climate* **20**, 53–69.
- Rossow WB, Mekonnen A, Pearl C, Goncalves W. 2013 Tropical precipitation extremes. *J. Climate* **26**, 1457–1466.
- Muller C. 2013 Impact of convective organization on the response of tropical precipitation extremes to warming. *J. Climate* **26**, 5028–5043.
- Bao J, Sherwood SC, Colin M, Dixit V. 2017 The robust relationship between extreme precipitation and convective organization in idealized numerical modeling simulations. *J. Adv. Model Earth. Syst.* **9**, 2291–2303.
- Pendergrass AG. 2020 Changing degree of convective organization as a mechanism for dynamic changes in extreme precipitation. *Curr. Clim. Change Rep.* **6**, 47–54.
- Kendon EJ, Roberts NM, Fowler HJ, Roberts MJ, Chan SC, Senior CA. 2014 Heavier summer downpours with climate change revealed by weather forecast resolution model. *Nat. Clim. Change* **4**, 570–576.
- Ban N, Schmidli J, Schär C. 2015 Heavy precipitation in a changing climate: Does short-term summer precipitation increase faster? *Geophys. Res. Lett.* **42**, 1165–1172.
- Prein AF, Rasmussen RM, Ikeda K, Liu C, Clark MP, Holland GJ. 2017 The future intensification of hourly precipitation extremes. *Nat. Clim. Change* **7**, 48–52.
- Stevens B, Satoh M, Auger L, Biercamp J, Bretherton CS, Chen X, Düben P, Judt F, Khairoutdinov M, Klocke D, et al. 2019 DYAMOND: The DYnamics of the Atmospheric general circulation Modeled On Non-hydrostatic Domains. *Prog. Earth Planet. Sci.* **6**, 61.
- Satoh M, Stevens B, Judt F, Khairoutdinov M, Lin SJ, Putman WM, Düben P. 2019 Global cloud-resolving models. *Curr. Clim. Change Rep.* **5**, 172–184.
- Kuang Z, Blossey PN, Bretherton CS. 2005 A new approach for 3D cloud-resolving simulations of large-scale atmospheric circulation. *Geophys. Res. Lett.* **32**, L02809.
- Garner ST, Frierson DMW, Held IM, Pauluis O, Vallis GK. 2007 Resolving convection in a global hypohydrostatic model. *J. Atmos. Sci.* **64**, 2061–2075.
- Boos WR, Fedorov A, Muir L. 2016 Convective self-aggregation and tropical cyclogenesis under the hypohydrostatic rescaling. *J. Atmos. Sci.* **73**, 525–544.
- Fedorov AV, Muir L, Boos WR, Studholme J. 2019 Tropical cyclogenesis in warm climates simulated by a cloud-system resolving model. *Clim. Dyn.* **52**, 107–127.

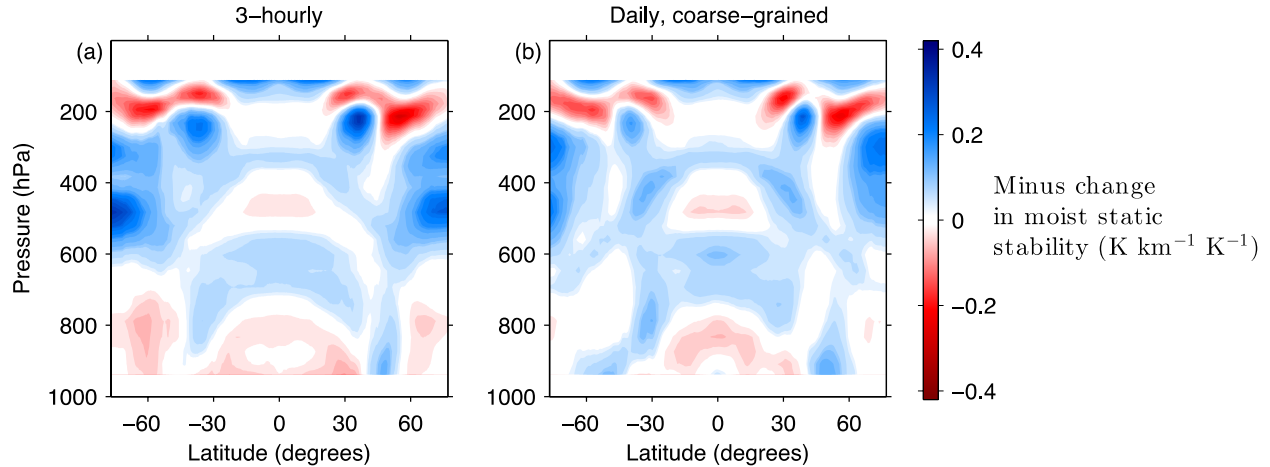
19. Hsieh TL, Garner ST, Held IM. 2020 Hypohydrostatic simulation of a quasi-steady baroclinic cyclone.
J. Atmos. Sci. **77**, 1415–1428.
20. Ma D, Boos W, Kuang Z. 2014 Effects of orography and surface heat fluxes on the South Asian summer monsoon.
J. Climate **27**, 6647–6659.
21. Pearson KJ, Lister GMS, Birch CE, Allan RP, Hogan RJ, Woolnough SJ. 2014 Modelling the diurnal cycle of tropical convection across the ‘grey zone’.
Quart. J. Roy. Meteor. Soc. **140**, 491–499.
22. Vellinga M, Roberts M, Vidale PL, Mizielinski MS, Demory ME, Schiemann R, Strachan J, Bain C. 2016 Sahel decadal rainfall variability and the role of model horizontal resolution.
Geophys. Res. Lett. **43**, 326–333.
23. Vergara-Temprado J, Ban N, Panosetti D, Schlemmer L, Schär C. 2020 Climate models permit convection at much coarser resolutions than previously considered.
J. Climate **33**, 1915–1933.
24. O’Gorman PA, Schneider T. 2009 Scaling of precipitation extremes over a wide range of climates simulated with an idealized GCM.
J. Climate **22**, 5676–5685.
25. Lu J, Leung LR, Yang Q, Chen G, Collins WD, Li F, Hou ZJ, Feng X. 2014 The robust dynamical contribution to precipitation extremes in idealized warming simulations across model resolutions.
Geophys. Res. Lett. **41**, 2971–2978.
26. Romps DM. 2011 Response of tropical precipitation to global warming.
J. Atmos. Sci. **68**, 123–138.
27. Singh MS, O’Gorman PA. 2015 Increase in moist-convective updraught velocities with warming in radiative-convective equilibrium.
Quart. J. Roy. Meteor. Soc. **141**, 2828–2838.
28. Singh MS, O’Gorman PA. 2013 Influence of entrainment on the thermal stratification in simulations of radiative-convective equilibrium.
Geophys. Res. Lett. **40**, 4398–4403.
29. Romps DM. 2016 Clausius–Clapeyron scaling of CAPE from analytical solutions to RCE.
J. Atmos. Sci. **73**, 3719–3737.
30. Singh MS, Kuang Z, Maloney ED, Hannah WM, Wolding BO. 2017 Increasing potential for intense tropical and subtropical thunderstorms under global warming.
Proc. Natl. Acad. Sci. **114**, 11657–11662.
31. Loriaux JM, Lenderink G, de Roode SR, Siebesma AP. 2013 Understanding convective extreme precipitation scaling using observations and an entraining plume model.
J. Atmos. Sci. **70**, 3641–3655.
32. Muller CJ, O’Gorman PA, Back LE. 2011 Intensification of precipitation extremes with warming in a cloud resolving model.
J. Climate **24**, 2784–2800.
33. O’Gorman PA. 2015 Precipitation extremes under climate change.
Curr. Clim. Change Rep. **1**, 49–59.
34. Tandon NF, Xuebin Z, Sobel AH. 2018 Understanding the dynamics of future changes in extreme precipitation intensity.
Geophys. Res. Lett. **45**, 2870–2878.
35. Nie J, Sobel AH, Shaevitz DA, Wang S. 2018 Dynamic amplification of extreme precipitation sensitivity.
Proc. Natl. Acad. Sci. **115**, 9467–9472.
36. Nie J, Dai P, Sobel AH. 2020 Dry and moist dynamics shape regional patterns of extreme precipitation sensitivity.
Proc. Natl. Acad. Sci. **117**, 8757–8763.
37. Li Z, O’Gorman PA. 2020 Response of vertical velocities in extratropical precipitation extremes to climate change.
Journal of Climate **33**, 7125–7139.
38. Khairoutdinov MF, Randall DA. 2003 Cloud resolving modeling of the ARM summer 1997 IOP: Model formulation, results, uncertainties, and sensitivities **60**, 607–625.
39. Kiehl JT, Hack JJ, Bonan GB, Boville BA, Williamson DL, Rasch PJ. 1998 The National Center for Atmospheric Research community climate model: CCM3.

- J. Climate* **11**, 1131–1149.
40. Kurowski MJ, Grabowski WW, Smolarkiewicz PK. 2015 Anelastic and compressible simulation of moist dynamics at planetary scales.
J. Atmos. Sci. **72**, 3975–3995.
41. Neale RB, Hoskins BJ. 2000 A standard test for AGCMs including their physical parametrizations: I: The proposal.
Atmos. Sci. Lett. **1**, 101–107.
42. Yuval J, O’Gorman PA. 2020 Stable machine-learning parameterization of subgrid processes for climate modeling at a range of resolutions.
Nature Commun. **11**, 3295.
43. Ballinger AP, Merlis TM, Held IM, Zhao M. 2015 The sensitivity of tropical cyclone activity to off-equatorial thermal forcing in aquaplanet simulations.
J. Atmos. Sci. **72**, 2286–2302.
44. Möbis B, Stevens B. 2012 Factors controlling the position of the Intertropical Convergence Zone on an aquaplanet.
J. Adv. Model Earth. Syst. **4**, M00A04.
45. Bretherton CS, Khairoutdinov MF. 2015 Convective self-aggregation feedbacks in near-global cloud-resolving simulations of an aquaplanet.
J. Adv. Model Earth. Syst. **7**, 1765–1787.
46. Kharin VV, Zwiers FW, Zhang X, Hegerl GC. 2007 Changes in temperature and precipitation extremes in the IPCC ensemble of global coupled model simulations.
J. Climate **20**, 1419–1444.
47. Quinn KM, Neelin JD. 2017 Distributions of tropical precipitation cluster power and their changes under global warming. Part I: Observational baseline and comparison to a high-resolution atmospheric model.
J. Climate **30**, 8033–8044.
48. Huffman GJ, Adler RF, Bolvin DT, Gu G, Nelkin EJ, Bowman KP, Hong Y, Stocker EF, Wolff DB. 2007 The TRMM multisatellite precipitation analysis (TMPA): Quasi-global, multiyear, combined-sensor precipitation estimates at fine scales.
J. Hydrometeorol. **8**, 38–55.
49. Kay JE, Deser C, Phillips A, Mai A, Hannay C, Strand G, Arblaster JM, Bates SC, Danabasoglu G, Edwards J, Holland M, Kushner P, Lamarque JF, Lawrence D, Lindsay K, Middleton A, Munoz E, Neale R, Oleson K, Polvani L, Vertenstein M. 2015 The community earth system model (CESM) large ensemble project: A community resource for studying climate change in the presence of internal climate variability.
Bull. Amer. Meteor. Soc. **96**, 1333–1349.
50. Chen CT, Knutson T. 2008 On the verification and comparison of extreme rainfall indices from climate models.
J. Climate **21**, 1605–1621.
51. Singh MS, O’Gorman PA. 2014 Influence of microphysics on the scaling of precipitation extremes with temperature.
Geophys. Res. Lett. **41**, 6037–6044.
52. Shi X, Durran DR. 2015 Estimating the response of extreme precipitation over mid-latitude mountains to global warming.
J. Climate **28**, 4246–4262.
53. Fildier B, Parishani H, Collins W. 2017 Simultaneous characterization of mesoscale and convective-scale tropical rainfall extremes and their dynamical and thermodynamic modes of change.
J. Adv. Model Earth. Syst. **9**, 2103–2119.
54. Abbott TH, Cronin TW, Beucler T. 2020 Convective dynamics and the response of precipitation extremes to warming in radiative–convective equilibrium.
J. Atmos. Sci. **77**, 1637–1660.
55. Fildier B, Parishani H, Collins WD. 2018 Prognostic power of extreme rainfall scaling formulas across space and time scales.
J. Adv. Model Earth. Syst. **10**, 3252–3267.
56. Marelle L, Myhre G, Hodnebrog Ø, Sillmann J, Samset BH. 2018 The changing seasonality of extreme daily precipitation.
Geophys. Res. Lett. **45**, 11352–11360.

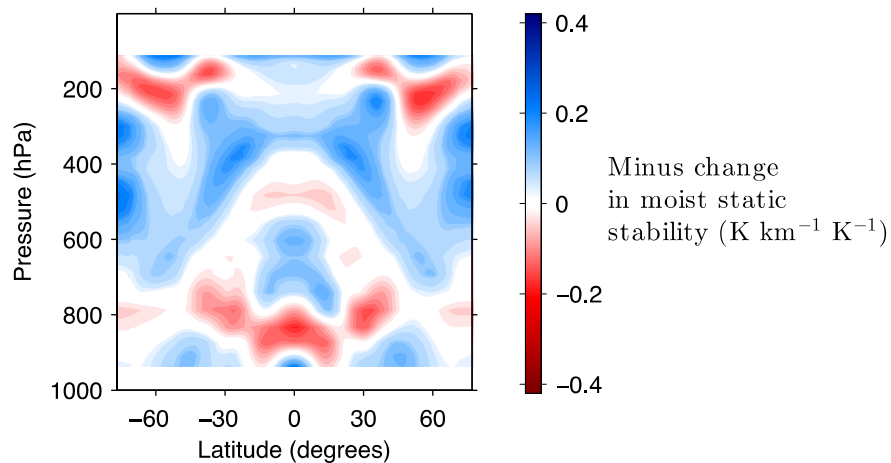
57. Singh MS, O'Gorman PA. 2012 Upward shift of the atmospheric general circulation under global warming: Theory and simulations **25**, 8259–8276.
58. O'Gorman PA, Dwyer JG. 2018 Using machine learning to parameterize moist convection: Potential for modeling of climate, climate change, and extreme events. *J. Adv. Model. Earth. Syst.* **10**, 2548–2563.
59. Rasp S, Pritchard MS, Gentine P. 2018 Deep learning to represent sub-grid processes in climate models. *Proc. Natl. Acad. Sci.* **115**, 9684–9689.
60. Brenowitz ND, Bretherton CS. 2018 Prognostic validation of a neural network unified physics parameterization. *Geophys. Res. Lett.* **45**, 6289–6298.

Response of extreme precipitation to uniform surface warming in quasi-global aquaplanet simulations at high resolution

P.A. O'Gorman, Z. Li, W.R. Boos and J. Yuval



Supplementary Figure 1: Minus the change ($\text{K km}^{-1} \text{K}^{-1}$) in moist static stability associated with precipitation extremes in response to climate change for (a) 3-hourly precipitation extremes on the model grid and (b) daily precipitation that is spatially coarse-grained to a horizontal grid spacing of 96km prior to calculating the extremes. Changes are normalized by the increase in SST of 4K. Changes below 950hPa and above 100hPa are not shown. The same changes expressed as a percent of the control-climate values are shown in Fig. 5e,f in the main paper.



Supplementary Figure 2: Minus the change ($\text{K km}^{-1} \text{K}^{-1}$) in moist static stability calculated from the zonal- and time-mean temperature in response to climate change. Changes are normalized by the increase in SST of 4K. Changes below 950hPa and above 100hPa are not shown.